ACS Photonics

pubs.acs.org/journal/apchd5

Article

Efficient Analysis of Photoluminescence Images for the Classification of Single-Photon Emitters

Leah R. Narun, Rebecca E. K. Fishman, Henry J. Shulevitz, Raj N. Patel, and Lee C. Bassett*

Cite This: *ACS Photonics* 2022, 9, 3540−3549

Read Online

ACCESS | Metrics & More | Article Recommendations | Supporting Information

ABSTRACT: Solid-state single-photon emitters (SPE) are a basis for emerging technologies such as quantum communication and quantum sensing. SPE based on fluorescent point defects are ubiquitous in semiconductors and insulators, and new systems with desirable properties for quantum information science may exist among the vast number of unexplored defects. However, the characterization of new SPE typically relies on time-consuming techniques for identifying point sources by eye in photoluminescence (PL) images. This manual strategy is a bottleneck for discovering new SPE, motivating a more efficient method for characterizing emitters in PL images. Here, we present a quantitative method using image analysis and regression fitting to automatically identify Gaussian emitters in PL images and classify them according to their stability, shape, and intensity relative to the background. We demonstrate efficient emitter classification for SPE in nanodiamond arrays and hexagonal boron nitride flakes. Adaptive criteria detect SPE in both samples despite variation in emitter intensity, stability, and background features. The detection criteria can be tuned for specific material systems and experimental setups to accommodate the diverse properties of SPE.

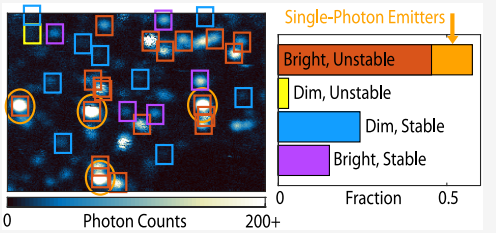

KEYWORDS: *single-photon emitters, photoluminescence, point defects, confocal microscopy, image analysis*

INTRODUCTION

Solid-state single-photon emitters (SPE) are a promising basis for future quantum technologies such as quantum computing,[1−4] sensing,[5,6] memory,[7,8] and communication.[9,10] Notable solid-state SPE systems include quantum dots[11−13] and fluorescent atomic defects within wide band-gap semiconductors such as diamond and silicon carbide.[14,15] More recently, interest has focused on two-dimensional (2D) materials such as hexagonal boron nitride (h-BN)[16−21] and transition-metal dichalcogenides.[22−24] There is no known ideal SPE system for all quantum applications, and even those that are suited for particular applications still come with trade-offs in their optical or material properties.[25] Improved SPE may emerge from the engineering of known systems or the discovery of new defects predicted by machine learning and ab initio calculations.[26,27] Many materials are mostly unexplored for SPE or in the initial stages of SPE investigation, including zinc sulfide,[28] zinc oxide,[29] titanium dioxide,[30] gallium nitride,[31] and colloidal quantum dots.[32]

Solid-state SPE are usually identified and characterized using confocal microscopy, which facilitates the isolation of optical-diffraction-limited features from background fluorescence in a three-dimensional sample. Typically, confocal microscopy images are analyzed by eye for features of interest. This manual procedure is sufficient for the study of a few emitters, but efforts to screen engineered defects or bulk crystals to study the SPE's formation or statistical properties underscore the need for an automatic detection method. Analyzing engineered defects created through ion implantation,[33−38] electron irradiation,[39,40] annealing,[41,42] or specialized growth schemes[22,43] often requires detecting hundreds of potential SPE. It is especially time consuming to investigate randomly located and often sparse emitters throughout three-dimensional (3D) bulk crystals, and a thorough evaluation of all potential emitters is crucial for characterizing a novel material with unknown defect populations.

Existing methods to characterize emitters in large-area PL images are primarily ensemble studies meant to assist manual detection. For instance, varying the excitation polarization of the PL image or applying a magnetic field highlights emitters with specific characteristics like potential spin states.[18] Similar methods have been used to probe non-linear excitation by comparing two-photon and continuous wave PL images[44] or by combining spectra and spatial intensity.[19] For materials with heterogeneous emitters, statistical modeling of the spatial distribution of emitter ensembles identifies defect families based on their intensity.[45] However, these methods do not yield quantitative information regarding the optical properties of individual SPE that can be used to classify or prioritize them

Received: May 25, 2022
Published: October 31, 2022

https://doi.org/10.1021/acsphotonics.2c00795
ACS Photonics 2022, 9, 3540−3549

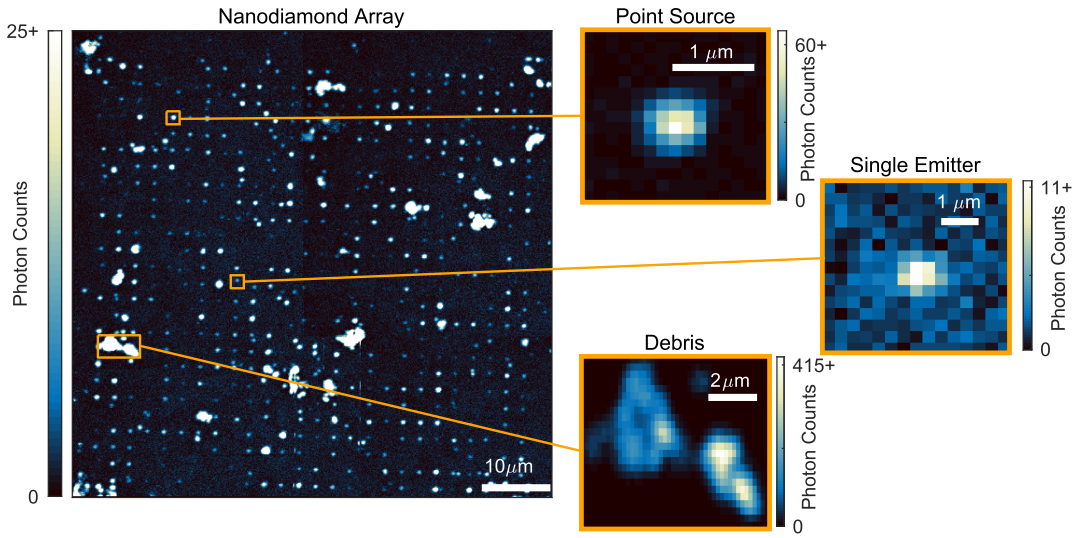

Figure 1. Stitched PL images of a nanodiamond array containing nitrogen-vacancy centers, acquired under 532 nm excitation.

for deeper investigation. Once individual SPE of interest are identified, well-established methods exist to characterize their spatial, spectral, and temporal emission characteristics. Examples of efficient characterization methods include wide-angle energy-momentum spectroscopy[46] and photon emission correlation spectroscopy.[47] Other methods to streamline the characterization of single-photon emitters on an individual level include machine learning to reduce the time measuring the second-order autocorrelation function.[48] However, still missing from the literature is a flexible emitter screening step to replace the manual identification of emitters in PL images, evaluating individual emitters while also maintaining a broad view of emitter properties.

To ensure broad applicability across material systems, an emitter screening method should leverage the known physics and optical properties of SPE in 2D PL images. All defect-based SPE appear as point sources in confocal PL images, the shape of which is determined by the microscope's point spread function. Ideally, the point spread function is a diffraction-limited Airy disk, but a 2D Gaussian function is typically an excellent approximation. The Gaussian width depends on the numerical aperture of the confocal microscope setup and the emission wavelength. Furthermore, SPE are not identical across material systems. Brightness and stability vary according to the characteristics of the defect and its host environment, with some emitters like those found in h-BN showing intermittent emission known as blinking.[49−53] Promising emitters may bleach temporarily or permanently with continued laser exposure.

Varying spatial distributions also create challenges for automatic detection. Multiple SPE can partially or completely overlap within the diffraction limit to yield a bright emitter that is indistinguishable by eye from true SPE.[54−57] While overlap is naturally expected for spatially inhomogeneous emitter distributions created by focused ion beams or contained in dispersed nanoparticles, emitters can cluster in apparently homogeneous samples due to invisible spatial variations in strain, composition, or extended structural defects. Hence, an apparently isolated emitter is not guaranteed to be a single emitter. In some cases, single emitters may be discerned using spectral filtering techniques,[58,59] but room temperature broadening of defects' emission spectra makes identification of SPE via spectroscopy alone impossible. Finally, experimental factors such as image resolution, dwell time, and background signal intensity can all affect the ability to detect emitters. Thus, the heterogeneity of SPE systems warrants a highly flexible image processing method to accommodate the wide range of SPE properties in PL images.

Here, we describe an automatic method that leverages the known optical properties of SPE to realize widely applicable screening criteria that emphasize Gaussian shape, diffraction-limited size, and sufficient signal-to-noise ratio. The method accounts for the common features found in experimental PL images such as Figure 1, which includes point sources, single emitters, background signals, and debris. Our method analyzes the entire image in Figure 1 in just 45 s, gathering quantitative information on each emitter's size, signal-to-noise ratio, and shape to classify emitters according to their stability and intensity. The expected emitter characteristics, where known, inform which emitter group to prioritize for detailed studies, such as measurement of the second-order photon autocorrelation function to confirm single emission. Because the method groups similar emitters, the properties of confirmed SPE help to further refine the search. The result is a method that minimizes human input and reduces the time spent in the object detection and second-order autocorrelation stages of SPE exploration. In addition to the array of nanodiamonds containing nitrogen-vacancy (NV) centers[60] shown in Figure 1, we apply the method to characterize SPE in exfoliated flakes of single-crystal h-BN. The two samples are characterized by markedly different SPE properties, in terms of their spatial distribution, brightness, stability, and signal-to-noise ratio, yet the method succeeds in rapidly classifying emitters in both cases.

METHODS

Data Acquisition and Sample Preparation. We use two custom-built confocal microscopes to image nanodiamond arrays containing NV centers[60] and exfoliated flakes of h-BN containing SPE. The microscopes feature continuous-wave excitation lasers operating at 532 and 592 nm, respectively. The nanodiamond PL image resolution is 100−150 nm with a scan rate of 400 Hz, while the h-BN PL image resolution is 50 nm with a scan rate of 100 Hz. Emitters dominated by single-

https://doi.org/10.1021/acsphotonics.2c00795
ACS Photonics 2022, 9, 3540−3549

photon emission (SPE) are confirmed by measuring the second-order photon autocorrelation function $g^{(2)}(\tau)$ and determining a zero-delay value $g^{(2)}(\tau = 0) < 0.5$ with background correction. This metric may overestimate the number of SPE,[47] but it serves as a threshold for emitters worthy of more detailed investigation. The empirical fit for $g^{(2)}(\tau)$ and example curves for SPE and non-SPE are given by eq 1 and Figures S1−S4, respectively, in the Supporting Information. Nanodiamonds are arranged in a grid with 2.6 μm spacing over a Si/SiO_2 substrate. 25 μm by 25 μm PL images of two nanodiamond arrays yield 189 emitters, 25 of which are deemed SPE. Bulk, single-crystal h-BN (acquired from HQ Graphene) is mechanically exfoliated into thin (<100 nm) flakes placed over a Si/SiO_2 substrate fabricated with 6−8 μm circular depressions recessed to a depth of 5 μm. The flakes are O_2 plasma-cleaned in an oxygen barrel asher at 50 W power and 50 sccm flow rate for 5 min. The samples are subsequently annealed in a tube furnace in an argon environment for 120 min at 850 °C. Emitters in h-BN are found around and within the recessed areas, and there are 8 verified SPE among two flakes.

Image Analysis. The method we describe is related to established spectroscopic techniques such as single particle tracking[61] and super-resolution microscopy,[62] which fit emitters with a Gaussian function. To start, 2D photoluminescence images are converted into binary images using an adaptive background threshold. The binary image is constructed by setting all pixels above or equal to the threshold to 1, while all pixels that are less than the threshold are set to 0. As opposed to a universal threshold, an adaptive threshold accounts for spatial variation in background intensity by calculating the local mean intensity for each pixel of the PL image.[63] Further explanation of adaptive thresholding and a comparison with a universal threshold (Figure S7) can be found in the Supporting Information. Using the binary image, interconnected foreground pixels that share at least an edge or a corner are identified as individual objects. Overlapping emitters are separated by local maximum detection using the PL image, and any objects smaller than the diffraction-limited spot size are discarded. Using object center positions from the binary image, each object is cropped from the full PL image into at least 15 by 15 pixel regions of interest (ROI). For larger objects, the ROI is the smallest rectangular box that fully contains the emitter in the binary image. Each detected object within the ROI is assigned a 2D Gaussian function within a simultaneous fit for all emitters plus a constant background. The minimum ROI area of 15 × 15 pixels ensures sufficient degrees of freedom in the 2D Gaussian fit for calculation of the goodness-of-fit parameter (introduced in the detection criteria section). The 2D symmetric Gaussian function is given by

$$I(x, y) = A \cdot \exp\left(-\frac{(x - x_0)^2 + (y - y_0)^2}{2\sigma^2}\right) \quad (1)$$

where A is the peak intensity of the emitter, (x_0, y_0) are the emitter coordinates, and σ is the emitter width, corresponding to the Gaussian standard deviation. The Gaussian fit provides the width, signal-to-noise ratio, and goodness-of-fit parameter for each emitter, which serve as the primary detection criteria.

Detection Criteria. *Width.* Objects are filtered based on their best-fit Gaussian width. For a diffraction-limited point source, the expected width is

$$\sigma_{\text{diff}} = 0.21\frac{\lambda}{\text{NA}} \quad (2)$$

where λ is the defect's emission wavelength and NA is the numerical aperture of the microscope objective.[64] If the emission wavelength is unknown, a width range can be estimated by substituting the microscope's detection range for λ. Typically, the detection range will be bound by the laser excitation wavelength and the upper limit of the photon detector's range. In practice, optical aberrations or nonideal confocal conditions may distort the microscope's point spread function, increasing the apparent width. This adjustment can often be calibrated using a multiplicative factor determined by comparison between the Gaussian function and the microscope's point spread function, measured using a known sample with a bright, stable point source. We constrain the best-fit width to a range, $\sigma \in [\sigma_{\text{min}}, \sigma_{\text{max}}]$, where σ_{min} and σ_{max} are set based on estimates for the expected Gaussian width corresponding to the wavelength range of interest and adjustments based on the microscope's point spread function.

2D Gaussian Fit. The symmetric 2D Gaussian fit filters the detected objects according to their shape, selecting for Gaussian point sources over misshapen and extended objects. The width constraint from the previous section is applied in this step as the range of allowed width for each peak in the fit. The emitter position is also tightly constrained to within 2 pixels of the weighted center of the detected object to ensure that partially overlapping emitters are fit separately. We perform a least-squares regression fit where the free parameters include the position, width, and amplitude of each emitter plus a constant background. The goodness-of-fit parameter is defined as reduced chi-squared (χ^2_{R}), given by

$$\chi^2_{\text{R}} = \frac{1}{\text{DoF}}\sum_{i=1}^{N}\frac{(O_i - M_i)^2}{\sigma_i^2} \quad (3)$$

in which M_i is the fitted counts, O_i is the measured counts, $\sigma_i = \sqrt{O_i}$ is the Poisson noise of the measured counts, and DoF is the number of degrees of freedom in the fit.

For an ideal fit with many degrees of freedom, χ^2_{R} equal to 1 means that the model fits the data within the expected variance, χ^2_{R} less than 1 indicates that the data is over-fitted by the model, and χ^2_{R} greater than 1 indicates a poor fit or a model that does not fully capture the data. The statistical expectation for a good fit depends on DoF, with bounds at $\chi^2_{\text{R}} = 1 \pm \sqrt{\frac{2}{\text{DoF}}}$. For ROIs containing 15 × 15 pixels and one emitter, the expected χ^2_{R} range based only on the degrees of freedom in the fit is 0.9−1.1. However, it is also necessary to account for sources of error in the confocal setup when setting the limits for χ^2_{R}. We have found that extending the allowed χ^2_{R} values on an empirical basis to 0.8 and 1.5 ensures that the Gaussian fit is robust against error in our confocal setup. The upper limit of 1.5 accounts for slight under-fitting due to the systematic error between our microscope's point spread function and the 2D Gaussian function. The lower limit of 0.8 reflects over-fitted emitters with low signal-to-noise ratio, which occurs when dim SPE are close to the background level. A more detailed explanation of confocal setup error and its effect on each of the detection criteria can be found in the Discussion section. A χ^2_{R} value less than 0.8 indicates objects that are usually background fluctuations and should be discarded. However, we find that a χ^2_{R} value much greater

https://doi.org/10.1021/acsphotonics.2c00795
ACS Photonics 2022, 9, 3540−3549

Table 1. Emitter Groups and Representative SPE Observed in PL Images of Nanodiamond Arrays and H-BN Flakes[a]

Group A	Group B	Group C	Group D
SNR > 10 $0.8 < \chi_R^2 < 1.5$ Width within limits	$2 < \mathrm{SNR} < 10$ $0.8 < \chi_R^2 < 1.5$ Width within limits	$2 < \mathrm{SNR} < 10$ $0.8 < \chi_R^2 < 1.5$ Width at limits	SNR > 10 $0 < e < 0.66$ Width within limits
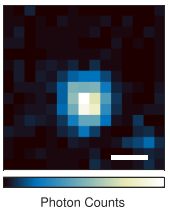	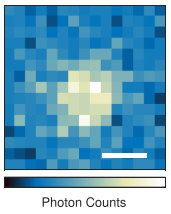	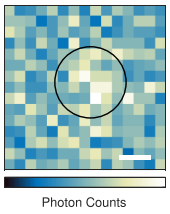	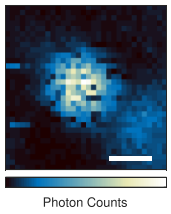
bright, stable	dim, stable	dim, blinking	bright, blinking

[a]SNR describes the brightness of the emitter with respect to the noise of the background. Reduced chi-squared (χ_R^2) is the goodness-of-fit parameter for the 2D Gaussian fit. The width refers to the Gaussian width calculated in the 2D Gaussian fit, while the limits are set according to the detection range of the confocal setup and the expected emission wavelength (if known). Eccentricity (e) is derived from the 2D elliptical Gaussian fit and replaces χ_R^2 as a measure of symmetry for bright and blinking emitters. The PL image examples shown for A and D are SPE in h-BN, while those shown for C and B are SPE from the nanodiamond array. PL counts are normalized to the maximum intensity of each image. Scale bars are 0.5 μm.

than 1.5 is possible for bright SPE affected by blinking and uneven PL image background. These emitters appear Gaussian and symmetric by eye except for a small number of dark pixels. An uneven background or bright background object can also produce a large χ_R^2 value. Dim emitters are less affected by these factors due to their lower contrast with the background.

Without an alternative measure, these bright, blinking emitters would be excluded on the basis of their high χ_R^2 value. For materials with emitters frequently affected by these issues, we find that emitter shape—specifically, elliptical eccentricity—is an effective means to filter point sources from extended objects. The elliptical 2D Gaussian function is defined as

$$I(x,y) = A\cdot \exp\left(-\left(\frac{\cos^2\theta}{2\sigma_1^2}+\frac{\sin^2\theta}{2\sigma_2^2}\right)\tilde{x}^2 + 2\left(\frac{\sin^2 2\theta}{4\sigma_1^2}-\frac{\sin^2 2\theta}{4\sigma_2^2}\right)\tilde{x}\tilde{y} - \left(\frac{\sin^2\theta}{2\sigma_1^2}+\frac{\cos^2\theta}{2\sigma_2^2}\right)\tilde{y}^2\right) \quad (4)$$

where A is the peak intensity, $(\tilde{x},\tilde{y}) = (x-x_0, y-y_0)$ are relative coordinates, σ_1 and σ_2 are the Gaussian widths of the elliptical axes, and θ is the rotation angle. The emitter eccentricity is defined as

$$e = \sqrt{1-\left(\frac{\min[\sigma_1,\sigma_2]}{\max[\sigma_1,\sigma_2]}\right)^2} \quad (5)$$

Possible eccentricity values range from 0 for a circle to 1 for a line. We set the allowed range of eccentricity for SPE detection to any value between 0 and 0.66, corresponding to at least a 3:4 ratio between the minor and major widths. For bright emitters in materials known to have uneven background and frequent blinking, eccentricity overrides χ_R^2 in classifying SPE. Because the elliptical Gaussian fit must be used in addition to the symmetric Gaussian fit, it doubles the computation time of the method and thus should be reserved only for materials with bright and unstable emitters. Additional guidance for when to use the elliptical Gaussian fit is provided in the Practical Use Considerations section.

Signal-to-Noise Ratio. The signal-to-noise ratio (SNR) is incorporated into the detection criteria to avoid the selection of dim, under-fitted emitters that are likely to be fluctuations in the background. The SNR is given by

$$\mathrm{SNR} = \frac{A}{\sqrt{B}} \quad (6)$$

where A is the best-fit emitter intensity and B is the best-fit background value. The SNR depends on both the emitter brightness and the acquisition settings (particularly the dwell time per pixel). An alternative approach could use the signal-to-background ratio, which is less dependent on the acquisition settings; however, we find that SNR is more robust in identifying SPE by incorporating both the emitter intensity and its statistical significance as an emitter defined above the background level. We set a lower limit of SNR > 2 for emitter detection and a threshold of SNR = 10 to divide bright (SNR > 10) and dim (SNR < 10) emitters.

Emitter Classification. The detection criteria described in the previous section define four groups of emitters exhibiting qualitatively different characteristics. Table 1 lists the SNR, χ_R^2, and width criteria corresponding to each emitter group, along with representative example images. All emitters classified in groups A–D are consistent with Gaussian point sources. The groups are designed to capture similar emitters, reflecting common factors that affect PL images of SPE, like emitter instability and uneven background. Group A describes well-isolated, stable, bright objects, representing the ideal case for SPE discovery. Group B emitters are identical to group A, except they are dim. Group C describes emitters with a good Gaussian fit but unexpectedly large or small width, which often occurs for dim and blinking emitters. Group D captures well-sized and -shaped emitters for which background conditions or high frequency blinking significantly affects χ_R^2. By categorizing potential emitters in this manner, basic knowledge of the sample can direct further investigation into the most promising group.

https://doi.org/10.1021/acsphotonics.2c00795
ACS Photonics 2022, 9, 3540−3549

RESULTS

The automatic detection method was developed and tested using nanodiamonds and h-BN to span the range of emitter and background properties for SPE in PL images. The nanodiamond array features regularly spaced emitters placed at approximately the same depth. The NV centers contained in the nanodiamonds are stable, homogeneous, and well-known SPE, and they provide a baseline for the ideal case of stable, well-isolated emitters over an even background. However, stochastic distribution of NV centers within the nanodiamonds means that most emitters contain multiple NV centers. In contrast, emitters in h-BN are more uniformly spatially distributed, whereas they are frequently unstable and heterogenous, and the flake itself may vary in thickness over the imaging area. The method accommodates both extremes.

Figure 2 depicts the application of this method to the nanodiamond array. Figure 2A demonstrates the efficacy of the

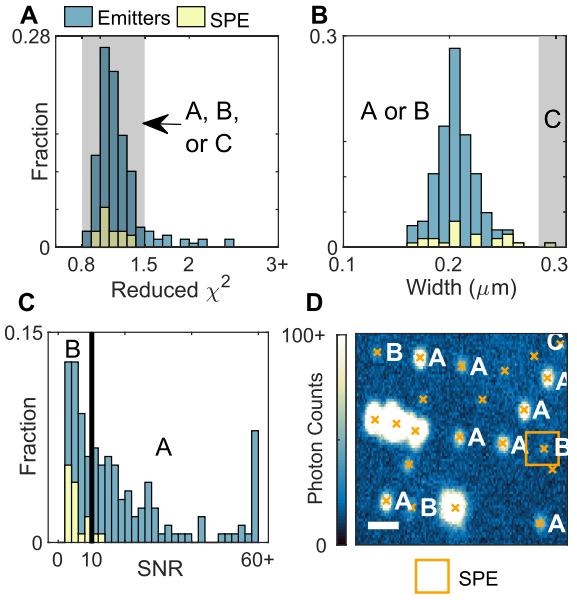

Figure 2. Emitter detection applied to 2D photoluminescence images of nanodiamond arrays. Blue bars show the given property distribution for all detected emitters that meet the criteria for one of the groups. The yellow bars show the given property distribution for SPE. (A) χ^2_R distribution, where the gray box shades the 0.8−1.5 range allowed for groups A, B, and C. (B) Gaussian width distribution for emitters within the allowed χ^2_R range demonstrates how most non-SPE are Gaussian point sources for this sample. The shaded box labeled "C" marks the SPE with fitted width very close to the upper width limit of 0.3 μm. (C) SNR distribution of emitters within the allowed χ^2_R range, showing intensity difference between SPE and non-SPE. The black line marks the chosen separation between "bright" and "dim" emitters at SNR equal to 10. (D) Object detection (orange "x") and group classification of emitters (white letters) according to Table 1 for a portion of a nanodiamond array. Group A is bright and stable, group B is dim and stable, group C is dim and blinking, and group D is bright and blinking. Scale bar is 2 μm.

chosen χ^2_R range in identifying SPE, and it further highlights how many objects in this sample are similarly well-shaped point sources but not SPE. Figure 2B demonstrates how almost all emitters in the nanodiamond array fall well within the chosen width limits, set as 100−300 nm to accommodate noise and systematic errors in the confocal setup. One SPE reaches the width limits and falls into group C (dim, unstable), suggesting that at least one SPE is too dim to be properly fit by the 2D Gaussian with the current PL image settings. Figure 2B also clarifies the extent of systematic error in our confocal setup. The approximate Gaussian width for a single NV center should be 152 nm, calculated using eq 2 for 690 nm peak emission with 532 nm excitation[65] and NA equal to 0.95. However, the average Gaussian width in Figure 2B for NV centers in our confocal setup is 205 nm, with ∼97% of emitters falling within ±40 nm of the mean. This error reflects the discrepancy between our microscope's point spread function and the ideal diffraction limit and motivates the extended width range. The final step, shown in Figure 2C, is to differentiate stable emitters based on intensity into groups A (bright, stable) and B (dim, stable). Due to the stability of the NV centers in this sample and the low, uniform background of the silicon substrate, these images do not benefit from the elliptical Gaussian fit, which is designed to gauge symmetry for blinking emitters or emitters over uneven background. Therefore, group D (bright, blinking) is not required.

Figure 3 displays the image analysis and emitter classification for an h-BN flake imaged with a 592 nm laser. The PL scan in

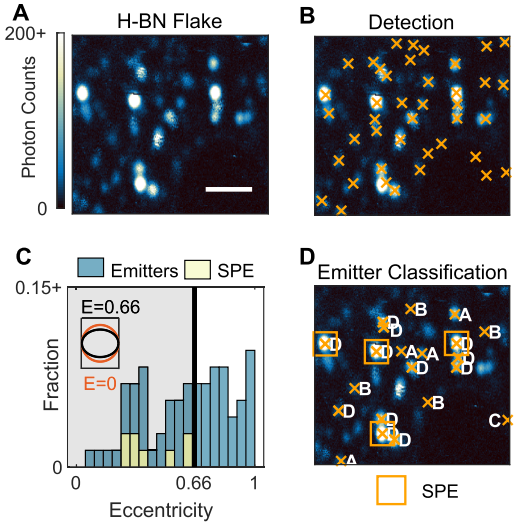

Figure 3. Emitter detection for hexagonal boron nitride flake. Scale bar is 2.5 μm. (A) PL image acquired under 592 nm excitation at 245 μW. Scale bar is 1 μm. (B) Object detection with adaptive thresholding. An orange "x" marks each detected object. (C) Distribution of eccentricity according to the elliptical Gaussian fit for SPE and other emitters found in two h-BN flakes, including the flake pictured in A and Figure S5 of the Supporting Information. The blue bars show the eccentricity distribution for all detected emitters that meet the criteria for one of the groups. The yellow bars denote the eccentricity distribution for SPE. The vertical black line and gray shaded region mark the allowed eccentricity range of 0−0.66 for group D. The inset shows a circle with eccentricity equal to zero (orange) and an ellipse with eccentricity equal to 0.66 (black). (D) Emitter classification of the objects detected in B according to groups outlined in Table 1. Group A is bright and stable, group B is dim and stable, group C is dim and blinking, and group D is bright and blinking.

Figure 3A shows overlapping and blinking emitters with an uneven background. Extended non-circular background objects of varying intensity are also visible in Figure 3A and sometimes overlap with potential Gaussian emitters. In Figure 3B, the object detection step using adaptive thresholding identifies possible emitters despite these nonidealities. The prevalence of

https://doi.org/10.1021/acsphotonics.2c00795
ACS Photonics 2022, 9, 3540−3549

blinking emitters in this sample motivates the use of shape analysis via the eccentricity criteria to capture symmetric but unstable emitters. In Figure 3C, we show the eccentricity distribution for the emitters detected in this sample along with the threshold, $e < 0.66$. Notably, more than half (~55%) of detected emitters fall outside this range and are excluded on the basis of likely being emitter clusters or extended objects. Figure 3D labels only emitters retained by the analysis with their classification type; the image shows a dominance of group D, demonstrating the utility of including eccentricity as a secondary shape measure for capturing unstable emitters that would otherwise be excluded. Width, SNR, and χ^2_R distributions for h-BN are shown in Figure S6 of the Supporting Information.

The fluorescent defects in h-BN are generally heterogeneous in structure and feature a range of emission wavelengths.[66] Thus, the emission wavelength cannot be estimated consistently to give the expected size of a diffraction-limited spot. Width limits are set instead according to the detection range of the setup, determined by the 645 nm long wave pass filter in the setup and the decline of the photon detector efficiency at ~1000 nm. This range corresponds to 150−233 nm emitter width using eq 2, and the width limits are set from 100 to 350 nm to reflect the empirically broadened distribution revealed in the nanodiamond data (Figure 2B).

Figure 4 summarizes the performance of the method for the nanodiamond and h-BN data. For each sample, we plot the distribution of emitters grouped in each classification (including those that were excluded) and indicate the number of SPE. For both samples, the emitters excluded or cut show a low likelihood of being SPE. The gray bars and gray scatter plot points in Figure 4 indicate the emitters cut by the method because they do not meet any group's criteria. 0% of cut emitters are SPE for h-BN, and 13% of cut emitters are SPE for the nanodiamonds. The higher percentage for the nanodiamonds reflects 3 very dim (SNR < 2) SPE among just 23 discarded emitters of 189 detected in the nanodiamond arrays. The uncertainty in the predicted concentration of SPE within each group is given by the Wilson interval[67] to reflect the statistical uncertainty based on the number of emitters within each group.

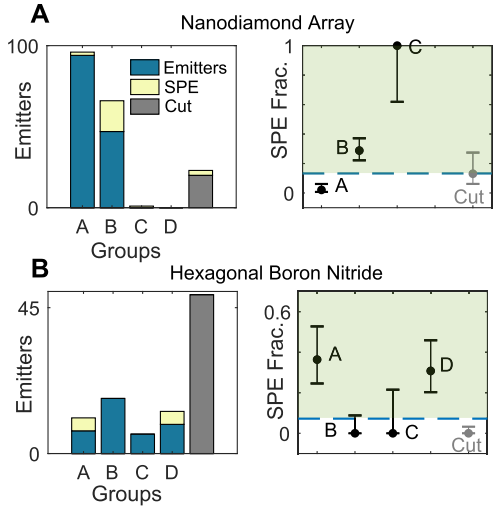

Figure 4. SPE distribution for group A (bright and stable), group B (dim and stable), group C (dim and unstable), and group D (bright and unstable) for (A) nanodiamond arrays and (B) h-BN samples. Blue bars show all emitters detected in the PL image and assigned to a group. Gray bars show emitters detected in the PL image that are "cut" and not assigned to a group. Yellow bars show the portion of the blue or gray bars that are SPE. Blue dashed line denotes the total fraction of SPE for all emitters detected, including those that are cut (0.132 for nanodiamonds and 0.072 for h-BN). The gray data points toward the right labeled "cut" reflect the SPE fraction for the gray bars. Error bars indicate the Wilson confidence interval.

The emitter groups substantially improve the probability of finding SPE compared to random sampling of all potential emitters. For the nanodiamond arrays, 13% of all emitters are SPE, but group B contains 29% SPE. Indeed, SPE are expected to be relatively dim and stable (group B) in this sample since most nanodiamonds contain more than one NV center. The three discarded SPE in the nanodiamond data are within the χ^2_R range but show a very low SNR of less than 2. Such low SNR indicates an emitter that would be very difficult to detect by eye. For the h-BN sample, only 7% of all potential emitters are SPE, but groups A and D each contain over 30% SPE. Notably, many bright and stable emitters (group A) in h-BN are not single emitters, suggesting a higher degree of emitter clustering than would be expected for randomly distributed defects. Group C is the least common for both the nanodiamonds and h-BN samples, which is reflected in the large uncertainty range in Figure 4. It is important to consider the uncertainty before using SPE fraction as a probability estimate of finding SPE in that group for a material. For the nanodiamonds, just one emitter classified in group C means that there is a large uncertainty in the SPE fraction. However, the presence of 1 SPE in group C out of 25 SPE in the nanodiamond array suggests that it may be useful to adjust the PL image settings to better capture dim emitters. Additional explanation of the limited number of emitters in group C is reserved for the Discussion section.

DISCUSSION

Accounting for Sample, Emitter, and Setup Variation. The detection criteria we describe are rooted in the fundamental optical properties of fluorescent defects, but in practice, there are several systematic and random sources of error that cause the measured PL of the emitter to stray from the theoretical ideal. It is necessary to understand and anticipate error to tailor the method to unique materials and setups.

Systematic error sources include the microscope's point spread function, position-dependent optical aberrations, and material-specific properties like high or uneven background and blinking emitters. Random error originates from the Poisson noise of the measured counts and is exacerbated by low PL image acquisition time and resolution. The method accounts for these errors by expanding the limits of the detection criteria and tolerating false positives to ensure that very few SPE are missed. The specific error implications for the width, Gaussian fit, and SNR criteria are discussed in this section.

Width. The width criterion is strongly affected by setup-dependent factors that create a discrepancy between the fitted Gaussian width and the expected size of a diffraction-limited spot. In the nanodiamond sample, for example, the expected spot size in our confocal setup is between 117 and 233 nm, as calculated from eq 2, with λ bounded by the laser excitation (532 nm) and the upper limit of the photon detector (1000 nm). However, confirmed SPE in the nanodiamond arrays

https://doi.org/10.1021/acsphotonics.2c00795
ACS Photonics 2022, 9, 3540−3549

display widths between 100 and 300 nm (Figure 2B). Systematic broadening can be quantified by comparing a known point source like the NV center with the Gaussian point spread function, providing a scaling factor for the expected width. However, without time-consuming, high-resolution PL images, the large width variance due to random error still prevents a strict width limit. In practice, it is also likely that emission wavelength of each emitter will initially be unknown. In this case, the most effective strategy is to screen for emitters that are reasonably within the diffraction limit given the error of the setup. The broad width limits applied for the nanodiamond and h-BN samples ensured that no SPE were missed and successfully filtered small background fluctuations and large, extended objects.

Any emitters that comply with the SNR and χ^2_R criteria but reach the imposed width limits require special consideration. An emitter is said to reach the width limits if its fitted width is within 1 nm of the imposed limits. These emitters are typically dim and blinking, presenting as just a few bright pixels or a partial 2D Gaussian point spread function. Blinking SPE may still be well fit by the 2D Gaussian point spread function if the emitter is close to the background level, but the width may not accurately reflect the emitter. Thus, low SNR emitters with unusual widths are isolated into group C to prioritize emitter stability and acknowledge that in rare cases, the width-limited fit may not fully describe the emitter. The failure of the 2D Gaussian fit to ascertain the width is more likely to occur in PL images of lower quality, unlike the PL images of the nanodiamonds and h-BN that are already highly optimized. Therefore, by definition, group C is less likely to occur than other groups for the emitters in the PL images in this paper. Still, it is necessary to include group C in the event that a dim SPE is not properly fit by the Gaussian function. Group C can also include dim and poorly defined background spots, demonstrated for the h-BN data in Figure S6 of the Supporting Information.

Goodness of Fit. The inherent discrepancy between the microscope's point spread function and the 2D Gaussian fitting function shifts the expected χ^2_R, even for a perfect point source. In our confocal setup, we account for this discrepancy by moving the upper limit of χ^2_R to 1.5, which is higher than the limit predicted on purely statistical grounds. This limit of 1.5 is likely applicable to other setups with similar acquisition settings unless there is a high degree of shape distortion visible by eye. The precise upper limit may be adjusted once a sample of known SPE is acquired and fit. Similarly, while the 0−0.66 eccentricity range used to define group D reflects the properties of our confocal microscope, this range will likely be reasonable for another well-aligned setup. It is also possible to reduce the allowed range of eccentricity to define a more selective group D.

The selectivity of the Gaussian fit is strongly impacted by material characteristics such as poor background, low signal-to-noise ratio ($2 < SNR < 5$), and blinking. Blinking points and uneven background bias the Gaussian fit because each point's contribution to χ^2_R is weighted by the inverse of the variance of the measured photon counts. Therefore, a poor fit among dim background or blinking points disproportionately worsens χ^2_R, with blinking SPE in h-BN sometimes showing χ^2_R up to 30. Group D captures bright and symmetric emitters that would be otherwise missed by the method because of background or blinking effects.

Signal-to-Noise Ratio. The SNR criterion is least affected by both setup and material sources of error; however, they do depend somewhat on the acquisition settings. The SNR computation relies on the Gaussian fit for the peak intensity of the emitter and background level, but these parameters are accurate if the fit is constrained to the emitter and the initial background condition is reasonable. In our images, the definitions of bright ($SNR > 10$) and dim ($2 < SNR < 10$) successfully separate most point sources from single-photon emitters in the nanodiamond sample as shown in Figure 2C. These limits also distinguish bright, blinking emitters in h-BN (Figure 3) for classification as group D. Similar limits are likely applicable to any material system, as they describe the emitter's relation to the background as it pertains to the detection criteria. For example, any bright emitter over a locally uneven background will benefit from the width ratio calculation to double-check the circularity. If needed, the precise thresholds can be adjusted to reflect the overall confocal image SNR as determined by its resolution and dwell time.

PRACTICAL USE CONSIDERATIONS

When applying the method to a particular sample, the objective is to determine which group will be the best to prioritize for SPE search. Systems with stable, isolated, and high intensity emitters, including color centers in diamond and quantum dots, will tend to exhibit SPE in the stable and bright group A. For ion-implanted samples or fabricated nanoparticle arrays, defects are naturally clustered within diffraction-limited areas. Thus, SPE are more likely to be found in the dim C and B groups than the bright A and D groups. Samples of this type include the nanodiamond arrays, etched arrays of nanopillars[68] and nanopyramids,[69] and ion-implanted arrays. A high occurrence of emitter blinking should guide the user to implement the group D categorization based on shape, especially if there are very few emitters categorized as the bright and stable group A. H-BN is a prominent example of blinking emitters, but other examples include nanocrystals[70,71] and certain quantum dots.[72]

For lesser-known or entirely new samples, it is more difficult to predict the expected characteristics of SPE. However, basic knowledge of the sample can provide some guidance to prioritize autocorrelation measurements for certain groups. First, the user should determine the applicability of group D, as the elliptical Gaussian fit approximately doubles the time to apply the method. Group D should be used only if initial large-area PL images show a high frequency of blinking or if the method discards most emitters with only groups A−C. Even if group D is engaged, group A emitters should probably take precedence for measurements because their stability and high signal-to-noise ratio will enable shorter acquisition times. Group D emitters could be investigated next, since these emitters also exhibit high signal-to-noise ratios. However, if the user expects emitter overlap within the diffraction limit, the dim and stable group B should be prioritized for potential SPE instead of group A or D. Group C should likely be investigated last, as dim and blinking emitters do not generally possess favorable properties for SPE. If many emitters are classified as group C, it may be helpful to adjust the PL image dwell time, resolution, or laser power to improve the imaging of dim emitters. For samples with no expectation of overlapping emitters, the dim groups B and C will contain emitters that are close to the background and require long autocorrelation acquisition times.

https://doi.org/10.1021/acsphotonics.2c00795
ACS Photonics 2022, 9, 3540−3549

The group criteria presented in this paper grant useful information on the distribution of key emitter properties such as intensity and stability. However, in the case of in-depth study of a single material system, it may be useful to fine-tune the emitter groups by incorporating observed properties of known SPE. As mentioned previously, the key obstacle to stricter group criteria is the intrinsic error in the confocal setup. Because SNR is least affected by setup error, refining the SNR criteria can be accomplished with a small number of known SPE. Quantifying an SNR range for SPE in a specific material system will be particularly useful to filter spots that likely contain more than one emitter within the diffraction limit. Fine-tuning the width, eccentricity, or reduced chi-squared criteria can also improve the SPE fraction of the emitter groups but will require a deeper understanding of factors like local optical aberrations and the microscope's unique PSF, which distort the shape and size of SPE. It may also be useful to alter the number of groups by either combining existing groups or creating new subgroups. For example, if all known SPE are considered bright (SNR > 10), it would be more beneficial to forgo the dim SPE groups and instead further subdivide the bright groups. Creating groups with different SNR or width ranges within the bright classification would help determine if there are variations in SPE properties due to multiple defect families present in the material.

This method is designed to identify diffraction-limited point sources, and thus, a high prevalence of false positives is largely dependent on emitter spatial clustering. For instance, the high rate of nanodiamond false positives shown in Figure 4 is expected because the NV centers are naturally confined within sub-diffraction (~40 nm-diameter) particles. Acquisition settings are also important in the method's efficacy, and a certain amount of trial-and-error can help to optimize the performance. Low PL image resolution can lead to false positives that are only background fluctuations. In general, the PL image resolution should be no larger than the mean of the expected width range. Resolution at half the mean of the expected width or below is recommended for samples with unstable, crowded emitters over an inconsistent background. Photo-bleaching the sample can also help reduce the background and the occurrence of false positives.

CONCLUSIONS

The method presented in this paper provides a general, flexible framework for efficiently screening new materials for SPE. Compared to manual searching, the ability to detect and classify individual fluorescent emitters through quick image processing greatly improves the speed of exploratory experiments. While we have demonstrated the utility of this method for commonly studied defect hosts like h-BN and diamond, it can also be applied to promising yet largely unexplored materials. Potential new hosts include compound semiconductors like magnesium and strontium oxides, group II–VI materials like zinc sulfide, complex metal oxides like yttrium orthosilicate, and perovskites.[25] While we consider two-dimensional confocal images of planar samples, the method can be readily adapted to detect emitters distributed within three-dimensional samples. This can be accomplished by automating acquisition of PL maps through different planes and performing sequential or simultaneous analysis of each image. In addition to investigating new SPE, the emitter detection and characterization method can also generally enhance knowledge of the defect and material system by providing quantitative information about the emitter spatial locations, brightness, and shape. For instance, the correlation of defects' optical properties and positions can establish relationships between the existence and properties of SPE with grain boundaries, growth sectors, or other material features. The process to optimize ion-implantation dose and energy for single defect creation is also improved by efficient detection and characterization of large emitter arrays. The method could also be adapted to classify emitters based on additional spectral, temporal, or polarization-dependent information that is acquired through more advanced imaging techniques. In summary, this method for rapid characterization of emitters in PL images will advance the discovery and study of new defects for quantum technology applications, and it can help to expand the collective knowledge of quantum defects and the material factors that influence their properties.

ASSOCIATED CONTENT

Supporting Information

The Supporting Information is available free of charge at https://pubs.acs.org/doi/10.1021/acsphotonics.2c00795.

Select $g^2(\tau)$ curves and photoluminescence images for nanodiamond emitters and width, SNR, and χ^2_R distributions of h-BN flakes (PDF)

AUTHOR INFORMATION

Corresponding Author

Lee C. Bassett − *Quantum Engineering Laboratory, Department of Electrical and Systems Engineering, University of Pennsylvania, Philadelphia, Pennsylvania 19104, United States;* orcid.org/0000-0001-8729-1530; Email: lbassett@seas.upenn.edu

Authors

Leah R. Narun − *Quantum Engineering Laboratory, Department of Electrical and Systems Engineering, University of Pennsylvania, Philadelphia, Pennsylvania 19104, United States; Department of Materials Science and Engineering, University of Pennsylvania, Philadelphia, Pennsylvania 19104, United States;* orcid.org/0000-0001-7501-937X

Rebecca E. K. Fishman − *Quantum Engineering Laboratory, Department of Electrical and Systems Engineering, University of Pennsylvania, Philadelphia, Pennsylvania 19104, United States; Department of Physics and Astronomy, University of Pennsylvania, Philadelphia, Pennsylvania 19104, United States;* orcid.org/0000-0001-8271-7125

Henry J. Shulevitz − *Quantum Engineering Laboratory, Department of Electrical and Systems Engineering, University of Pennsylvania, Philadelphia, Pennsylvania 19104, United States;* orcid.org/0000-0001-9298-8519

Raj N. Patel − *Quantum Engineering Laboratory, Department of Electrical and Systems Engineering, University of Pennsylvania, Philadelphia, Pennsylvania 19104, United States;* orcid.org/0000-0003-1634-1208

Complete contact information is available at: https://pubs.acs.org/10.1021/acsphotonics.2c00795

Funding

This work was supported by the National Science Foundation under Award DMR-1922278. L.R.N. acknowledges support from the University Scholars Program at the University of Pennsylvania. H.J.S. and L.C.B. acknowledge support from

NSF through the University of Pennsylvania Materials Research Science and Engineering Center (MRSEC) (DMR-1720530) to develop the nanodiamond arrays used in this study.

Notes

The authors declare no competing financial interest.

Computer code giving an example of the image processing, object detection, 2D Gaussian fitting, and emitter classification described in this paper is available at https://github.com/penn-qel/PL-classify.git.

■ ACKNOWLEDGMENTS

We thank Tzu-Yung Huang for helpful discussions about optical aberrations and image processing.

■ REFERENCES

(1) Childress, L.; Hanson, R. Diamond NV centers for quantum computing and quantum networks. *MRS Bull.* **2013**, *38*, 134−138.
(2) Liu, X.; Hersam, M. C. 2D materials for quantum information science. *Nat. Rev. Mater.* **2019**, *4*, 669−684.
(3) Jiang, L.; Taylor, J. M.; Sørensen, A. S.; Lukin, M. D. Distributed quantum computation based on small quantum registers. *Phys. Rev. A* **2007**, *76*, 062323−062355.
(4) Atatüre, M.; Englund, D.; Vamivakas, N.; Lee, S. Y.; Wrachtrup, J. Material platforms for spin-based photonic quantum technologies. *Nat. Rev. Mater.* **2018**, *3*, 38−51.
(5) Degen, C. L.; Reinhard, F.; Cappellaro, P. Quantum sensing. *Rev. Mod. Phys.* **2017**, *89*, 035002−035041.
(6) Schirhagl, R.; Chang, K.; Loretz, M.; Degen, C. L. Nitrogen-vacancy centers in diamond: Nanoscale sensors for physics and biology. *Annu. Rev. Phys. Chem.* **2014**, *65*, 83−105.
(7) Heshami, K.; England, D. G.; Humphreys, P. C.; Bustard, P. J.; Acosta, V. M.; Nunn, J.; Sussman, B. J. Quantum memories: emerging applications and recent advances. *J. Mod. Opt.* **2016**, *63*, 2005−2028.
(8) Bradley, C. E.; Randall, J.; Abobeih, M. H.; Berrevoets, R. C.; Degen, M. J.; Bakker, M. A.; Markham, M.; Twitchen, D. J.; Taminiau, T. H. A Ten-Qubit Solid-State Spin Register with Quantum Memory up to One Minute. *Phys. Rev. X* **2019**, *9*, 031045−031057.
(9) Gao, W. B.; Imamoglu, A.; Bernien, H.; Hanson, R. Coherent manipulation, measurement and entanglement of individual solid-state spins using optical fields. *Nat. Photonics* **2015**, *9*, 363−373.
(10) Wehner, S.; Elkouss, D.; Hanson, R. Quantum internet: A vision for the road ahead. *Science* **2018**, *362*, No. eaam9288.
(11) Arakawa, Y.; Holmes, M. J. Progress in quantum-dot single photon sources for quantum information technologies: A broad spectrum overview. *Appl. Phys. Rev.* **2020**, *7*, 021309−021325.
(12) Somaschi, N.; et al. Near-optimal single-photon sources in the solid state. *Nat. Photonics* **2016**, *10*, 340−345.
(13) Loredo, J. C.; et al. Scalable performance in solid-state single-photon sources. *Optica* **2016**, *3*, 433−440.
(14) Aharonovich, I.; Englund, D.; Toth, M. Solid-state single-photon emitters. *Nat. Photonics* **2016**, *10*, 631−641.
(15) Wolfowicz, G.; Heremans, F. J.; Anderson, C. P.; Kanai, S.; Seo, H.; Gali, A.; Galli, G.; Awschalom, D. D. Quantum guidelines for solid-state spin defects. *Nat. Rev. Mater.* **2021**, *6*, 906−925.
(16) Tran, T. T.; Bray, K.; Ford, M. J.; Toth, M.; Aharonovich, I. Quantum emission from hexagonal boron nitride monolayers. *Nat. Nanotechnol.* **2016**, *11*, 37−41.
(17) Koperski, M.; Nogajewski, K.; Potemski, M. Single photon emitters in boron nitride: More than a supplementary material. *Opt. Commun.* **2018**, *411*, 158−165.
(18) Exarhos, A. L.; Hopper, D. A.; Patel, R. N.; Doherty, M. W.; Bassett, L. C. Magnetic-field-dependent quantum emission in hexagonal boron nitride at room temperature. *Nat. Commun.* **2019**, *10*, 222.
(19) Stern, H. L.; Wang, R.; Fan, Y.; Mizuta, R.; Stewart, J. C.; Needham, L. M.; Roberts, T. D.; Wai, R.; Ginsberg, N. S.; Klenerman, D.; Hofmann, S.; Lee, S. F. Spectrally Resolved Photodynamics of Individual Emitters in Large-Area Monolayers of Hexagonal Boron Nitride. *ACS Nano* **2019**, *13*, 4538−4547.
(20) Reserbat-Plantey, A.; Epstein, I.; Torre, I.; Costa, A. T.; Gonçalves, P. A.; Mortensen, N. A.; Polini, M.; Song, J. C.; Peres, N. M.; Koppens, F. H. Quantum Nanophotonics in Two-Dimensional Materials. *ACS Photonics* **2021**, *8*, 85−101.
(21) Azzam, S. I.; Parto, K.; Moody, G. Prospects and challenges of quantum emitters in 2D materials. *Appl. Phys. Lett.* **2021**, *118*, 240502−240513.
(22) Palacios-Berraquero, C.; Kara, D. M.; Montblanch, A. R.-P.; Barbone, M.; Latawiec, P.; Yoon, D.; Ott, A. K.; Loncar, M.; Ferrari, A. C.; Atatüre, M. Large-scale quantum-emitter arrays in atomically thin semiconductors. *Nat. Commun.* **2017**, *8*, 15093.
(23) Chakraborty, T.; Lehmann, F.; Zhang, J.; Borgsdorf, S.; Wöhrl, N.; Remfort, R.; Buck, V.; Köhler, U.; Suter, D. CVD growth of ultrapure diamond, generation of NV centers by ion implantation, and their spectroscopic characterization for quantum technological applications. *Phys. Rev. Mater.* **2019**, *3*, 065205−065216.
(24) Dang, J.; Sun, S.; Xie, X.; Yu, Y.; Peng, K.; Qian, C.; Wu, S.; Song, F.; Yang, J.; Xiao, S.; Yang, L.; Wang, Y.; Rafiq, M. A.; Wang, C.; Xu, X. Identifying defect-related quantum emitters in monolayer WSe_2. *npj 2D Mater. Appl.* **2020**, *4*, 2.
(25) Bassett, L. C.; Alkauskas, A.; Exarhos, A. L.; Fu, K. M. C. Quantum defects by design. *Nanophotonics* **2019**, *8*, 1867−1888.
(26) Frey, V. B.; Akinwande, N. C.; Jariwala, D.; Shenoy, D. Machine learning-enabled design of point defects in 2d materials for quantum and neuromorphic information processing. *ACS Nano* **2020**, *14*, 13406−13417.
(27) Ferrenti, A. M.; de Leon, N. P.; Thompson, J. D.; Cava, R. J. Identifying candidate hosts for quantum defects via data mining. *npj Comput. Mater.* **2020**, *6*, 126.
(28) Stewart, C.; Kianinia, M.; Previdi, R.; Tran, T. T.; Aharonovich, I.; Bradac, C. Quantum emission from localized defects in zinc sulfide. *Opt. Lett.* **2019**, *44*, 4873−4876.
(29) Linpeng, X.; Viitaniemi, M. L. K.; Vishnuradhan, A.; Kozuka, Y.; Johnson, C.; Kawasaki, M.; Fu, K.-M. C. Coherence Properties of Shallow Donor Qubits in ZnO. *Phys. Rev. Appl.* **2018**, *10*, 064061−064070.
(30) Chung, K.; Leung, Y. H.; To, C. H.; Djurišić, A. B.; Tomljenovic-Hanic, S. Room-temperature single-photon emitters in titanium dioxide optical defects. *Beilstein J. Nanotechnol.* **2018**, *9*, 1085−1094.
(31) Berhane, A. M.; Jeong, K. Y.; Bodrog, Z.; Fiedler, S.; Schröder, T.; Triviño, N. V.; Palacios, T.; Gali, A.; Toth, M.; Englund, D.; Aharonovich, I. Bright Room-Temperature Single-Photon Emission from Defects in Gallium Nitride. *Adv. Mater.* **2017**, *29*, 1605092−1605098.
(32) Kagan, C. R.; Bassett, L. C.; Murray, C. B.; Thompson, S. M. Colloidal Quantum Dots as Platforms for Quantum Information Science. *Chem. Rev.* **2021**, *121*, 3186−3233.
(33) Wang, C.; Kurtsiefer, C.; Weinfurter, H.; Burchard, B. Single photon emission from SiV centres in diamond produced by ion implantation. *J. Phys. B: At., Mol. Opt. Phys.* **2006**, *39*, 37−41.
(34) Toyli, D. M.; Weis, C. D.; Fuchs, G. D.; Schenkel, T.; Awschalom, D. D. Chip-scale nanofabrication of single spins and spin arrays in diamond. *Nano Lett.* **2010**, *10*, 3168−3172.
(35) Hollenbach, M.; Berencén, Y.; Kentsch, U.; Helm, M.; Astakhov, G. V. Engineering telecom single-photon emitters in silicon for scalable quantum photonics. *Opt. Express* **2020**, *28*, 26111−26121.
(36) Rodt, S.; Reitzenstein, S.; Heindel, T. Deterministically fabricated solid-state quantum-light sources. *J. Phys.: Condens. Matter* **2020**, *32*, 153003−153022.
(37) Klein, J.; et al.Scalable single-photon sources in atomically thin MoS2. Submitted 2020-02-20, arXiv (cond-mat.mes-hall). https://arxiv.org/abs/2002.08819v1 (accessed Dec 10, 2021).

https://doi.org/10.1021/acsphotonics.2c00795
ACS Photonics 2022, 9, 3540−3549

(38) Lagomarsino, S.; Flatae, A. M.; Kambalathmana, H.; Sledz, F.; Hunold, L.; Soltani, N.; Reuschel, P.; Sciortino, S.; Gelli, N.; Massi, M.; Czelusniak, C.; Giuntini, L.; Agio, M. Creation of Silicon-Vacancy Color Centers in Diamond by Ion Implantation. *Front. Phys.* **2021**, *8*, 601362.
(39) Fuchs, F.; Stender, B.; Trupke, M.; Simin, D.; Pflaum, J.; Dyakonov, V.; Astakhov, G. V. Engineering near-infrared single-photon emitters with optically active spins in ultrapure silicon carbide. *Nat. Commun.* **2015**, *6*, 7578−7584.
(40) Capelli, M.; Heffernan, A. H.; Ohshima, T.; Abe, H.; Jeske, J.; Hope, A.; Greentree, A. D.; Reineck, P.; Gibson, B. C. Increased nitrogen-vacancy centre creation yield in diamond through electron beam irradiation at high temperature. *Carbon* **2019**, *143*, 714−719.
(41) Xu, Z. Q.; et al. Single photon emission from plasma treated 2D hexagonal boron nitride. *Nanoscale* **2018**, *10*, 7957−7965.
(42) Lyu, C.; Zhu, Y.; Gu, P.; Qiao, J.; Watanabe, K.; Taniguchi, T.; Ye, Y. Single-photon emission from two-dimensional hexagonal boron nitride annealed in a carbon-rich environment. *Appl. Phys. Lett.* **2020**, *117*, 244002−244007.
(43) Kim, H.; Moon, J. S.; Noh, G.; Lee, J.; Kim, J. H. Position and Frequency Control of Strain-Induced Quantum Emitters in WSe_2 Monolayers. *Nano Lett.* **2019**, *19*, 7534−7539.
(44) Schell, A. W.; Tran, T. T.; Takashima, H.; Takeuchi, S.; Aharonovich, I. Non-linear excitation of quantum emitters in hexagonal boron nitride multiplayers. *APL Photonics* **2016**, *1*, 091302−091309.
(45) Breitweiser, S. A.; Exarhos, A. L.; Patel, R. N.; Saouaf, J.; Porat, B.; Hopper, D. A.; Bassett, L. C. Efficient Optical Quantification of Heterogeneous Emitter Ensembles. *ACS Photonics* **2020**, *7*, 288−295.
(46) Dodson, C. M.; Kurvits, J. A.; Li, D.; Zia, R. Wide-angle energy-momentum spectroscopy. *Opt. Lett.* **2014**, *39*, 3927−3930.
(47) Fishman, R. E. K.; Patel, R. N.; Hopper, D. A.; Huang, T.-Y.; Bassett, L. C.Photon emission correlation spectroscopy as an analytical tool for quantum defects. Submitted 2021-11-01, arXiv (quant-ph). https://arxiv.org/abs/2111.01252 (accessed May 24, 2022).
(48) Kudyshev, Z. A.; Bogdanov, S. I.; Isacsson, T.; Kildishev, A. V.; Boltasseva, A.; Shalaev, V. M. Rapid Classification of Quantum Sources Enabled by Machine Learning. *Adv. Quantum Technol.* **2020**, *3*, 2000067−2000074.
(49) van Dam, S. B.; Walsh, M.; Degen, M. J.; Bersin, E.; Mouradian, S. L.; Galiullin, A.; Ruf, M.; IJspeert, M.; Taminiau, T. H.; Hanson, R.; Englund, D. R. Optical coherence of diamond nitrogen-vacancy centers formed by ion implantation and annealing. *Phys. Rev. B* **2019**, *99*, 161203−161210.
(50) Chen, G.; Liu, Y.; Song, M.; Wu, B.; Wu, E.; Zeng, H. Photoluminescence enhancement dependent on the orientations of single NV centers in nanodiamonds on a gold film. *IEEE J. Sel. Top. Quantum Electron.* **2013**, *19*, 4602404−4602407.
(51) Cai, T.; Kim, J. H.; Yang, Z.; Dutta, S.; Aghaeimeibodi, S.; Waks, E. Radiative Enhancement of Single Quantum Emitters in WSe_2 Monolayers Using Site-Controlled Metallic Nanopillars. *ACS Photonics* **2018**, *5*, 3466−3471.
(52) Liu, Y.; Chen, G.; Rong, Y.; McGuinness, L. P.; Jelezko, F.; Tamura, S.; Tanii, T.; Teraji, T.; Onoda, S.; Ohshima, T.; Isoya, J.; Shinada, T.; Wu, E.; Zeng, H. Fluorescence Polarization Switching from a Single Silicon Vacancy Colour Centre in Diamond. *Sci. Rep.* **2015**, *5*, 12244.
(53) Gatto Monticone, D.; Traina, P.; Moreva, E.; Forneris, J.; Olivero, P.; Degiovanni, I. P.; Taccetti, F.; Giuntini, L.; Brida, G.; Amato, G.; Genovese, M. Native NIR-emitting single colour centres in CVD diamond. *New J. Phys.* **2014**, *16*, 053005−053022.
(54) Choi, S.; Tran, T. T.; Elbadawi, C.; Lobo, C.; Wang, X.; Juodkazis, S.; Seniutinas, G.; Toth, M.; Aharonovich, I. Engineering and Localization of Quantum Emitters in Large Hexagonal Boron Nitride Layers. *ACS Appl. Mater. Interfaces* **2016**, *8*, 29642−29648.
(55) Himics, L.; Tóth, S.; Veres, M.; Balogh, Z.; Koós, M. Creation of deep blue light emitting nitrogen-vacancy center in nanosized diamond. *Appl. Phys. Lett.* **2014**, *104*, 093101−093106.
(56) Schröder, T.; Trusheim, M. E.; Walsh, M.; Li, L.; Zheng, J.; Schukraft, M.; Sipahigil, A.; Evans, R. E.; Sukachev, D. D.; Nguyen, C. T.; Pacheco, J. L.; Camacho, R. M.; Bielejec, E. S.; Lukin, M. D.; Englund, D. Scalable focused ion beam creation of nearly lifetime-limited single quantum emitters in diamond nanostructures. *Nat. Commun.* **2017**, *8*, 15376.
(57) Thiruraman, J. P.; Masih Das, P.; Drndić, M. Irradiation of Transition Metal Dichalcogenides Using a Focused Ion Beam: Controlled Single-Atom Defect Creation. *Adv. Funct. Mater.* **2019**, *29*, 1904668−1904676.
(58) Kumar, S.; Kaczmarczyk, A.; Gerardot, B. D. Strain-Induced Spatial and Spectral Isolation of Quantum Emitters in Mono- and Bilayer WSe2. *Nano Lett.* **2015**, *15*, 7567−7573.
(59) Bertram, S. N.; Spokoyny, B.; Franke, D.; Caram, J. R.; Yoo, J. J.; Murphy, R. P.; Grein, M. E.; Bawendi, M. G. Single Nanocrystal Spectroscopy of Shortwave Infrared Emitters. *ACS Nano* **2019**, *13*, 1042−1049.
(60) Shulevitz, H. J.; Huang, T.-Y.; Xu, J.; Neuhaus, S. J.; Patel, R. N.; Choi, Y. C.; Bassett, L. C.; Kagan, C. R. Template-Assisted Self-Assembly of Fluorescent Nanodiamonds for Scalable Quantum Technologies. *ACS Nano* **2022**, *16*, 1847−1856.
(61) Manzo, C.; Garcia-Parajo, M. F. A review of progress in single particle tracking: From methods to biophysical insights. *Rep. Prog. Phys.* **2015**, *78*, 124601−124629.
(62) Schermelleh, L.; Ferrand, A.; Huser, T.; Eggeling, C.; Sauer, M.; Biehlmaier, O.; Drummen, G. P. Super-resolution microscopy demystified. *Nat. Cell Biol.* **2019**, *21*, 72−84.
(63) Bradley, D.; Roth, G. Adaptive Thresholding using the Integral Image. *Journal of Graphics Tools* **2007**, *12*, 13−21.
(64) Zhang, B.; Zerubia, J.; Olivo-Marin, J. C. Gaussian approximations of fluorescence microscope point-spread function models. *Appl. Opt.* **2007**, *46*, 1819−1829.
(65) Fukushige, K.; Kawaguchi, H.; Shimazaki, K.; Tashima, T.; Takashima, H.; Takeuchi, S. Identification of the orientation of a single NV center in a nanodiamond using a three-dimensionally controlled magnetic field. *Appl. Phys. Lett.* **2020**, *116*, 264002−264007.
(66) Exarhos, A. L.; Hopper, D. A.; Grote, R. R.; Alkauskas, A.; Bassett, L. C. Optical Signatures of Quantum Emitters in Suspended Hexagonal Boron Nitride. *ACS Nano* **2017**, *11*, 3328−3336.
(67) Wilson, E. B. Probable Inference, the Law of Succession, and Statistical Inference. *J. Am. Stat. Assoc.* **1927**, *22*, 209−212.
(68) McCloskey, D. J.; Dontschuk, N.; Broadway, D. A.; Nadarajah, A.; Stacey, A.; Tetienne, J. P.; Hollenberg, L. C.; Prawer, S.; Simpson, D. A. Enhanced Widefield Quantum Sensing with Nitrogen-Vacancy Ensembles Using Diamond Nanopillar Arrays. *ACS Appl. Mater. Interfaces* **2020**, *12*, 13421−13427.
(69) Jaffe, T.; Felgen, N.; Gal, L.; Kornblum, L.; Reithmaier, J. P.; Popov, C.; Orenstein, M. Deterministic Arrays of Epitaxially Grown Diamond Nanopyramids with Embedded Silicon-Vacancy Centers. *Adv. Opt. Mater.* **2019**, *7*, 1800715−1800722.
(70) Bradac, C.; Gaebel, T.; Naidoo, N.; Sellars, M. J.; Twamley, J.; Brown, L. J.; Barnard, A. S.; Plakhotnik, T.; Zvyagin, A. V.; Rabeau, J. R. Observation and control of blinking nitrogen-vacancy centres in discrete nanodiamonds. *Nat. Nanotechnol.* **2010**, *5*, 345−349.
(71) Nirmal, M.; Dabbousi, B. O.; Bawendi, M. G.; Macklin, J. J.; Trautman, J. K.; Harris, T. D.; Brus, L. E. Fluorescence intermittency in single cadmium selenide nanocrystals. *Nature* **1996**, *383*, 802−804.
(72) Davanço, M.; Hellberg, C. S.; Ates, S.; Badolato, A.; Srinivasan, K. Multiple time scale blinking in InAs quantum dot single-photon sources. *Phys. Rev. B* **2014**, *89*, 161303−161308.

https://doi.org/10.1021/acsphotonics.2c00795
ACS Photonics 2022, 9, 3540−3549